IOPscience iopscience.iop.org

Home Search Collections Journals About Contact us My IOPscience

Experimental quantum tomography of a homodyne detector

This content has been downloaded from IOPscience. Please scroll down to see the full text.

2017 New J. Phys. 19 053015

(http://iopscience.iop.org/1367-2630/19/5/053015)

View the table of contents for this issue, or go to the journal homepage for more

Download details:

IP Address: 155.198.12.188
This content was downloaded on 13/07/2017 at 18:51

Please note that terms and conditions apply.

You may also be interested in:

An Introduction to the Formalism of Quantum Information with Continuous Variables: Quantum information with continuous variables
C Navarrete-Benlloch

Recursive quantum detector tomography
Lijian Zhang, Animesh Datta, Hendrik B Coldenstrodt-Ronge et al.

Characterization of conditional state-engineering quantum processes by coherent state quantum process tomography
Merlin Cooper, Eirion Slade, Micha Karpiski et al.

Single-photon creation and annihilation operators
V Parigi, A Zavatta and M Bellini

Measuring measurement: theory and practice
A Feito, J S Lundeen, H Coldenstrodt-Ronge et al.

Tomography of photon-number resolving continuous-output detectors
Peter C Humphreys, Benjamin J Metcalf, Thomas Gerrits et al.

Data pattern tomography: reconstruction with an unknown apparatus
D Mogilevtsev, A Ignatenko, A Maloshtan et al.

Remote state preparation and teleportation in phase space
Matteo G A Paris, Mary Cola and Rodolfo Bonifacio

Improving information/disturbance and estimation/distortion trade-offs
Stefano Olivares and Matteo G A Paris

New Journal of Physics
The open access journal at the forefront of physics

Deutsche Physikalische Gesellschaft DPG
IOP Institute of Physics

Published in partnership with: Deutsche Physikalische Gesellschaft and the Institute of Physics

OPEN ACCESS

RECEIVED
29 December 2016

REVISED
21 April 2017

ACCEPTED FOR PUBLICATION
25 April 2017

PUBLISHED
17 May 2017

Original content from this work may be used under the terms of the Creative Commons Attribution 3.0 licence.

Any further distribution of this work must maintain attribution to the author(s) and the title of the work, journal citation and DOI.

PAPER

Experimental quantum tomography of a homodyne detector

Samuele Grandi[1,5], **Alessandro Zavatta**[2,3], **Marco Bellini**[2,3] **and Matteo G A Paris**[4]

[1] Centre for Cold Matter, Blackett Laboratory, Imperial College London, Prince Consort Road, SW7 2AZ London, United Kingdom
[2] Istituto Nazionale di Ottica (INO-CNR), I-50125 Florence, Italy
[3] LENS and Department of Physics and Astronomy, University of Florence, I-50019 Sesto Fiorentino, Florence, Italy
[4] Quantum Technology Lab, Dipartimento di Fisica, Università degli Studi di Milano, I-20133 Milano, Italy
[5] Author to whom any correspondence should be addressed.

E-mail: s.grandi@imperial.ac.uk

Keywords: quantum detector tomography, homodyne detector, quantum states of light

Abstract

We suggest and demonstrate a tomographic method to characterise homodyne detectors at the quantum level. The positive operator measure associated with the detector is expanded in a quadrature basis and probed with a set of coherent states. The coefficients of the expansion are then retrieved using a least squares algorithm. Our model is general enough to describe different implementations of the homodyne setup, and it has proven capable of effectively describing the detector response to different tomographic sets. We validate the reconstructed operator measure on nonclassical states and exploit results to estimate the overall quantum efficiency of the detector.

1. Introduction

Balanced homodyne detection is a crucial detection technique for continuous variable quantum technology and lies at the core of many experiments in fundamental quantum optics [1–3]. From its first proposal for the measurement of quadrature squeezing, to its current extensive use in the fields of quantum tomography, quantum communication and quantum metrology [4–18], this detection scheme has carved its place into experimental quantum optics. Besides quantum optical systems, homodyne detection extends its reach to the whole field of continuous variable quantum technologies, spanning from atomic systems [19, 20] to quantum optomechanics [21].

Advances in technology promoted the spread of many different configurations of this versatile apparatus, tailored to disparate experimental needs. Such a wide range of applications calls for reliable ways to fully characterise homodyne detectors at a quantum level. In fact, each specific setup so far relies on classical calibrations in order to gain the most general description of the apparatus and of the relationship between the input state and the measurement output. Recently, a characterisation of homodyne detection, however used only as a phase-insensitive photon counter, was demonstrated [22]. The detector characterisation made use of data pattern tomography, an alternative method to QDT [23]. Measurement data were directly interpreted using a direct fitting in terms of measurement outcomes to probe input states. Data pattern tomography has the advantage of easily describing many-outcome detectors. This comes at the cost of providing no information on the measurement process, a knowledge fundamental to push forward the control and the performance of the homodyne detector.

More generally, a reliable and robust model for the description of the fully phase-sensitive homodyne detection in the form of a quantum detector tomography (QDT) is, in fact, still lacking. Several CV quantum information protocols would largely benefit from a precise quantum description of the detector. In particular, in conditional-state preparation [24–28] a precise characterisation of homodyne detection would correspond to enhanced control on the quantum properties of the output signal.

The pioneering proposals for QDT [29–32] were followed by the experimental characterisation of an avalanche photodiode, in both single and time-multiplexed configurations, for the detection of up to eight photons [33]. Subsequent works developed the idea, including the effect of decoherence onto the operator

© 2017 IOP Publishing Ltd and Deutsche Physikalische Gesellschaft

description [34], or different detection devices, such as superconducting nanowires [35] and TES based systems [36, 37]. However, these are detectors devoted to photon counting, whose description is entirely embedded in the diagonal sector of the Fock space. Only recently, a specific phase-sensitive hybrid scheme, in the form of a weak homodyne detector based on photon counting, was the object of an experimentally realised QDT [38]. In this paper, we move several crucial steps forward, and present a theoretical and experimental realisation of QDT for homodyne detector, i.e. the most commonly used form of a fully phase-sensitive detector, whose detection operators are naturally described in phase space.

The quantum description of any detector is given by a positive operator-valued measure (POVM), i.e. a set of positive operators $\Pi = \{\Pi_n\}$, giving a resolution of identity $\sum_n \Pi_n = \mathbb{I}$. The determination of these operators is, in turn, the main goal of detector tomography. Given an input state ρ, the Born rule states that $p_n^\rho = \mathtt{Tr}\,[\rho\ \Pi_n]$ is the probability of obtaining the nth outcome when the generalised observable described by $\{\Pi_n\}$ is being measured. The inversion of this formula allows the reconstruction of the operators Π_n from the experimentally sampled probability distribution p_n^ρ, over a suitable set of known states ρ. These must form a tomographically complete set, spanning the Hilbert subspace where the POVM elements are defined on [39].

The simplest choice for a continuous variable system is a set of coherent states. They provide an over-complete basis for the Fock space, and it has already been proved that even one-dimensional discrete collections of coherent states form a complete basis, and may be used to reconstruct classical and non-classical states [40, 41]. In fact, the experimental distributions of the outcomes for a set of coherent states already provide a full representation of the detector operators, in the form of a sample of their Q-functions

$$Q_n(\alpha) = \frac{1}{\pi}\langle\alpha|\ \Pi_n\ |\alpha\rangle = \frac{1}{\pi}\,\mathcal{P}_n^\alpha,$$

where $\{\mathcal{P}_n^\alpha\}$ represents the probability distribution for a coherent state. However, this representation is not suitable to provide a complete and reliable *characterisation* of the detector. In fact, any subsequent use of this reconstruction scheme to *predict* the outcome of the measurement for a different signal would involve the (numerical) evaluation of the trace rule in the phase-space as

$$\mathtt{Tr}\,[\rho\ \Pi_n] = \int_{\mathbb{C}} \mathrm{d}^2\alpha\ P[\rho](\alpha)\,Q_n(\alpha),$$

where the Glauber–Sudarshan P-function $P[\rho](\alpha)$ is singular for any nonclassical state, and thus not ideal for sampling. The P-function could still be efficiently approximated, and it has been used successfully in characterisations of several optical processes [42–46].

In order to overcome this problem we suggest an expansion in the quadrature basis of the operator measure associated with the detector, using as probe a set of coherent states. We then obtain the coefficients of the expansion using a least squares algorithm on a sufficiently large sample of data. We also validate the experimentally obtained POVM by reconstructing nonclassical known states. Finally, we exploit results to estimate the overall quantum efficiency of the detector.

The paper is structured as follows. In section 2 we review the description of an ideal quantum homodyne detection and introduce the algorithm employed for the reconstruction of the POVM set of its realistic representation. In section 3 we describe our experimental apparatus, whereas in section 4 we present results of the reconstruction, as well as their validation on nonclassical states. Section 5 closes the paper with some concluding remarks.

2. Homodyne detection

An ideal homodyne detector is a fully phase sensitive apparatus that provides a complete characterisation of a given state of a single-mode radiation field [47]. This state, the *signal*, is sent to a balanced beam splitter, where it interferes with an intense coherent field, the local oscillator (LO), usually coming from the same laser source. The phase of the signal has then a precise value ϕ with respect to the local oscillator, and can be adjusted by means of a piezo-actuated mirror. The two outputs of the beam splitter are then focused on two photodiodes, and the resulting photocurrents subtracted and analysed. It can be shown that, in the approximation of high amplitude $|\beta|$ of the local oscillator, the measurement associated to this detector corresponds to

$$X = \frac{a\ \ b^\dagger + a^\dagger b}{2\ |\beta|} \underset{|\beta|\gg 1}{\longrightarrow} \frac{a^\dagger \mathrm{e}^{\mathrm{i}\phi} + a\ \mathrm{e}^{-\mathrm{i}\phi}}{2} = x_\phi, \tag{1}$$

where a and b are the mode operators for the signal and the LO, respectively. The operator b was replaced by $|\beta|\ \mathrm{e}^{\mathrm{i}\phi}$ in equation (1) by considering its action onto the LO, that can be treated as a coherent state $|\beta\rangle$. The operation connected to the working scheme of this detector is therefore the measurement of the quadrature operator x_ϕ on the signal mode. Such a link states the equivalence between the discrete spectrum of the operator

X and the continuous one of the quadrature, due to the high intensity of the LO, that can be consequently treated classically. This equivalence can be extended to the characteristic functions

$$\mathrm{Tr}_{a,b}[e^{i\lambda X}\rho \otimes |\beta\rangle\langle\beta|] \underset{|\beta|\gg 1}{\longrightarrow} \mathrm{Tr}_a[e^{i\lambda x_\phi}\rho] \tag{2}$$

assuring the equivalence of all moments [48].

The key feature of homodyne detection is its ability to discern between different phase values of an input signal, setting itself apart from the photon counting detectors that have been characterised in the past. A straightforward choice for a basis in which representing the POVM elements of a phase insensitive device is the number basis, in the form $\Pi_k = \sum_{n=0}^{+\infty} \pi_n^{(k)} |n\rangle\langle n|$, where $|n\rangle\langle n|$ is the projector onto the n-photon Fock state. Such a description is no longer suitable for our apparatus, that hinges on a phase-sensitive operation scheme. Off-diagonal elements in the number-basis expansion could enclose phase-sensitive properties, as was done in [38], but reconstruction of the detector operators would become increasingly difficult due to the high dimension of the Hilbert space the POVM would be defined in.

2.1. The reconstruction algorithm

A suitable basis to expand the POVM $\{\Pi(x)\}$ of a phase-sensitive detector for continuous variable systems is the set $\{|y\rangle\langle y|\}$ of projectors on eigenstates of the quadrature operator x_ϕ. Upon considering possible noise mechanisms, we may write

$$\Pi(x_\phi) = \int\int \mathrm{d}\varphi\, \mathrm{d}y\, G_\varphi^{(\phi)} g_y^{(x)} |y_\varphi\rangle\langle y_\varphi|. \tag{3}$$

In most cases the process of phase diffusion, described here by $G_\varphi^{(\phi)}$, is very limited, as we demonstrate for our setup in section 4.2. Under these assumptions, a convenient expansion to describe the effective POVM of the detector is diagonal in the quadrature basis, i.e. setting $\phi = 0$ and $G_\varphi^{(\phi)} = \delta(\varphi)$,

$$\Pi(x) = \int \mathrm{d}y\, g_y^{(x)} |y\rangle\langle y|. \tag{4}$$

We can use this equation as a starting point to model the physical realisation of a homodyne detector. At first, it is possible to move from a continuous set of POVM to a discrete one, reflecting the experimental sampling during the measurement process. In parallel, the expansion on the quadrature basis $\{|y\rangle\langle y|\}$ can be discretised as well, reducing the number of POVM elements. Equation (4) may be rewritten as

$$\Pi_j \equiv \Pi(x_j) = \sum_k g_k^j |y_k\rangle\langle y_k|, \tag{5}$$

where the indeces j and k are both confined to an arbitrary portion of phase space $[x_{\min}, x_{\max}]$. The function $g_k^{(x)}$ is now the matrix $\mathbf{g}$. A crucial feature of a homodyne detector is its response to amplitude. While the matrix $\mathbf{g}$ could incorporate this feature, it is preferable to decouple the two and add this response to the QDT as an additional parameter. We modelled this response with an amplitude dependent, positive parameter $\gamma(\alpha)$, whose action is to rescale the field amplitude measured by the detector. The Q-function representation of the detector is now given by

$$\mathcal{P}_{\alpha,\gamma}(x_j) = \langle\gamma\alpha|\,\Pi(x_j)|\gamma\alpha\rangle = \sum_k g_k^j \sqrt{\frac{2}{\pi}}\, \exp\{-2(y_k - \gamma|\alpha|)^2\}. \tag{6}$$

The QDT will associate to every detector a matrix $\mathbf{g}$ and a function $\gamma(\alpha)$, providing a complete and detailed description of the detector.

Equation (6) may be inverted to find the matrix $\mathbf{g}$ and the function $\gamma(\alpha)$, starting from a quorum set of known states. To this purpose, selecting a set of coherent states with amplitudes $\{\alpha_s\}$, we use a least-squares method to compare the detector outcomes with equation (6):

$$\mathbf{g} = \underset{\{g_k^j,\gamma_s\}>0}{\arg\min} \left\{ \sum_j \sum_s [p_{\alpha_s}(x_j) - P_{\alpha_s,\gamma_s}(x_j)]^2 \right\}, \tag{7}$$

where $p_{\alpha_s}(x_j)$ is the experimentally observed distribution for the coherent state with amplitude $|\alpha_s|$. The positivity of the $\{g_k^j\}$ is the sufficient condition for a POVM.

A pictorial representation of the algorithm is presented in figure 1(a). The algorithm retrieves $\mathbf{g}$ and $\{\gamma_s\}$ by comparing the experimentally sampled distributions to the corresponding Q-function representation. The least squares algorithm of equation (7) performs this minimisation simultaneously for all the quadrature values $x_j \in [x_{\min}, x_{\max}]$ and all the coherent states in the set. If we look back at equation (4), it is quite natural to link the characteristics of the matrix $\mathbf{g}$ to the features of the detector reconstruction. Each matrix row g_k^j associates an outcome x_j to a set of projectors on quadrature eigenstates, with weights given by the coefficients in equation (5). For an ideal detector, the matrix is diagonal $g_k^j = \delta_{kj}$, i.e. the only nonzero coefficient associates a quadrature

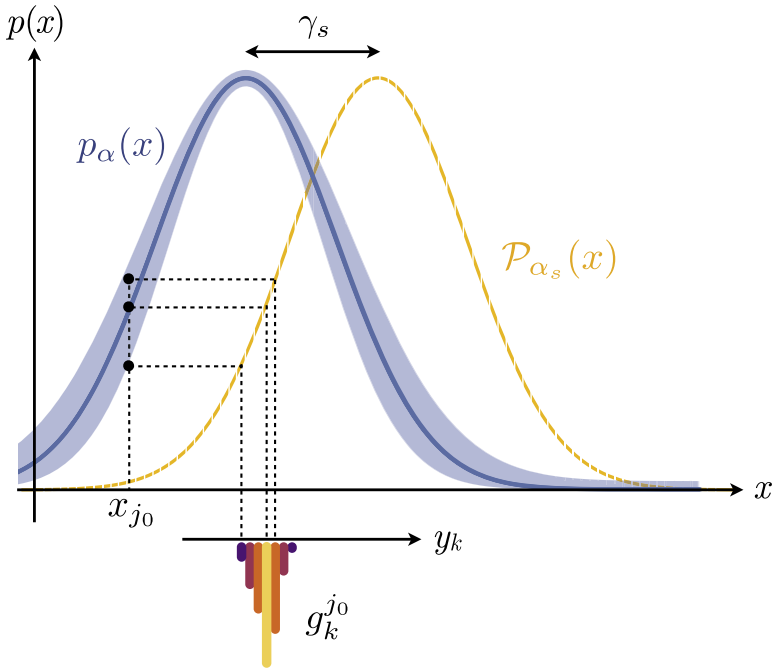

Figure 1. Quantum tomography of a homodyne detector. A pictorial representation of the least-squares algorithm is reported: the experimentally sampled probability distributions $p_\alpha(x)$ (solid blue) are compared to the Q-function representation $\mathcal{P}_\alpha(x)$ (dashed yellow). The dashing mirrors the discretisation of equation (4).

value x_j to the corresponding projector $|x_j\rangle\langle x_j|$. Experimental imperfections and fluctuations, corresponding to the shaded blue area in figure 1(a), 'switch on' new coefficients in the expansion of equation (6), spreading them around the central diagonal value. At the same time, each calibrated amplitude $|\alpha_s|$ is associated to a rescaled value $|\tilde{\alpha}_s| = \gamma_s\ |\alpha_s|$, providing a unified model for the amplitude response of the detector.

A detector tomography devised in this way is general enough for application to different configurations of the homodyne detection. In principle, every set $\{\gamma_s\}$ is valid only for one quadrature phase ϕ. In a broader context, the coefficients γ_s could be described by complex numbers, modifying the phase as well as the amplitude of every coherent state. However, we will show in the next section how, due to the robustness of the setup, in most cases our assumption of real γ_s can be verified.

3. Experimental apparatus

The detector characterised in this paper is an optical homodyne apparatus, operating in the time domain at high sampling frequency [49, 50]. A schematic diagram of the experimental setup is shown in figure 2. The apparatus is based on a mode-locked Ti:sapphire laser (Spectra-Physics Tsunami) providing, after suitable splitting, both the LO beam for balanced homodyne detection and the probe coherent states for detector tomography. The laser emits 2 ps pulses at a central wavelength of 785 nm, with a repetition rate of 82 MHz.

Amplitudes of the probe coherent states were selected by means of a reflective-coating glass attenuator. Precise calibration of each state is done by means of a Type I BBO crystal cut for degenerate spontaneous down-conversion (SPDC), pumped by the frequency doubled portion of the main laser beam. The injection of the probe coherent states into the signal path of the SPDC triggers the stimulated emission of downconverted photon pairs, in the same mode as the injection (thus generating single-photon-added coherent states SPACSs [51]), and in the idler mode. This emission rate is proportional to $1 + |\alpha|^2$, where α is the amplitude of the incoming coherent state. In order to generate pure quantum states, idler photons are strongly spectrally and spatially filtered before being detected with a single photon counting module. In this configuration, when the idler detector clicks, the signal state is prepared in a well-defined spatial/temporal mode defined by the SPDC pump beam [52]. Such a procedure provides a precise standard-free calibration of the input amplitude [53] by means of the ratio between the count rate of stimulated and spontaneous events, pursuing the idea of a calibration-free characterisation. The phase difference ϕ between the LO and the probe states identifies the quadrature x_ϕ measured by the homodyne detector. This is adjusted by means of a piezoelectric mirror in the LO path and it is actively stabilised to the desired value by a computer-assisted feedback loop.

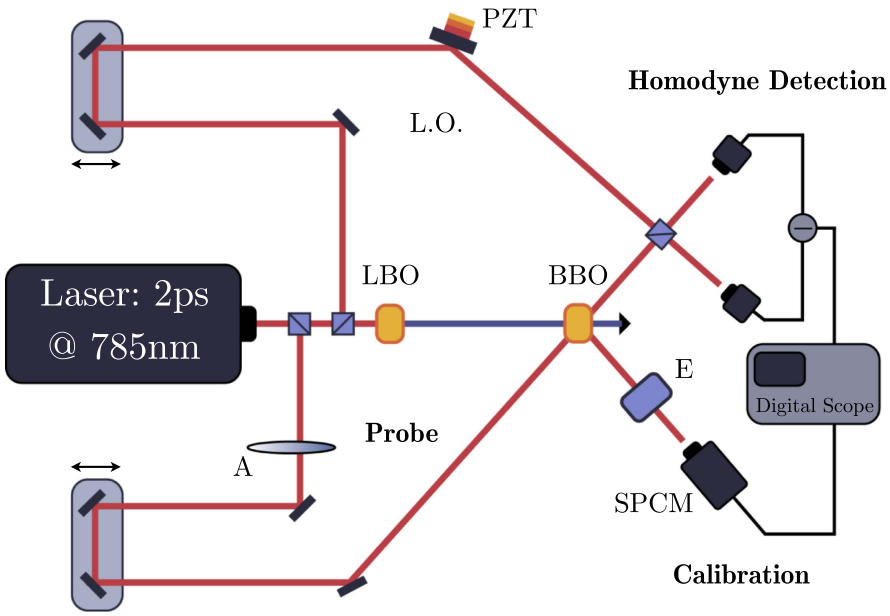

Figure 2. Schematic diagram of the experimental setup. L.O.: local oscillator. A: attenuator. LBO: frequency doubling crystal. BBO: down-conversion crystal. E: etalon filters. SPCM: single-photon counting module. PZT: piezoelectric mirror.

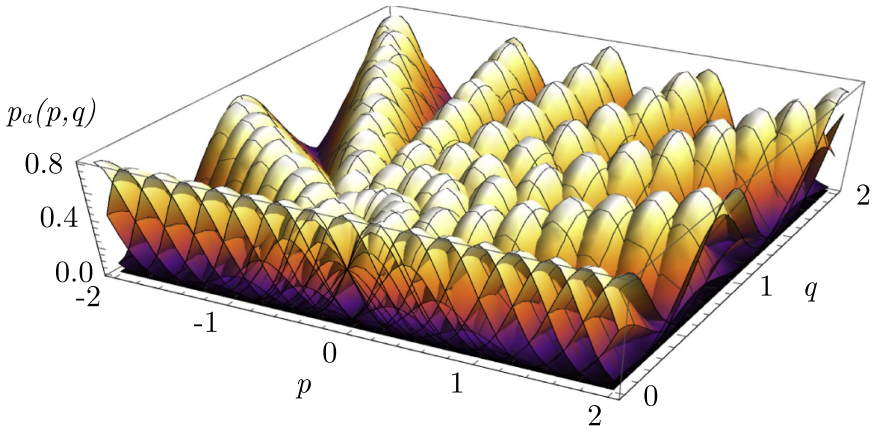

Figure 3. The theoretical phase space representation of the full set of coherent states used for tomography.

For each coherent probe state, the homodyne signal is acquired and integrated over a time interval corresponding to the duration of a laser pulse. The corresponding quadrature value is then calculated by normalising it to the vacuum noise, obtained when the homodyne signal beam is blocked. In order to avoid unwanted drifts of the homodyne signal, the measurements are taken in an ultra-stable configuration of the setup, and each coherent state acquisition is immediately followed by the vacuum acquisition needed for calibration, these two subsequent acquisitions are performed in a time sufficiently small in order to avoid undesirable dc-signal drifts. For every state, about 10^6 quadrature values are obtained, from which a probability distribution can be constructed. The detailed description of time-domain homodyne detection procedure, the calibration and the voltage-to-quadrature conversion are fully described in [49, 50].

4. Detector tomography

In our detector tomography we have focused attention to the range $x \in [-2,\ 2]$. To characterise this quadrature space we have selected a set of coherent states, with amplitudes $\alpha_s \in [0,\ 3]$. We selected 12 equally spaced amplitudes, the maximum achievable considering our calibration precision. For each amplitude we acquired 9 phase values between 0 and π. The tomographic set thus composed provides a uniform coverage of the selected portion of phase space, and provides a quorum for tomographies of a truncated Fock space of dimension $D = 9$ [54, 55]. The full set is represented in figure 3. Each state was measured following the procedure just described; it is important to notice that only the probability distribution $p_\alpha(x)$ with $x \in [-2,\ 2]$ takes part in the reconstruction algorithm.

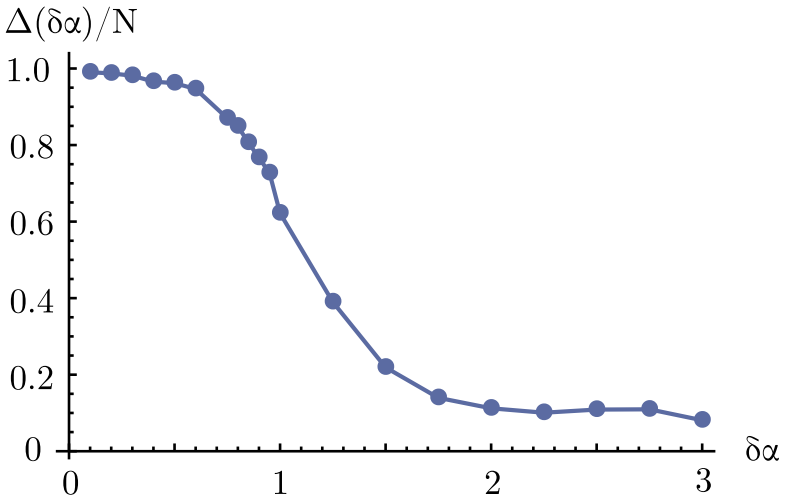

Figure 4. Efficiency of reconstruction as a function of increasing amplitude spacing in the tomographic set. The function $\Delta(\delta\alpha)$ is here normalised to the matrix dimension N. A sharp transition can be seen as the spacing between the states of the set approaches the maximum of the function $y \cdot f(y)$ where $f(y)$ is the overlap function defined in equation (9).

Before going to detector tomography we now focus on the properties of the tomographic set, and in particular on the characteristics required to perform a reliable and robust reconstruction. We start by analysing the resolution properties and then pass to check the robustness against phase and amplitude noise.

4.1. Properties of the tomographic set: resolution

In order to analyse the resolution properties of the tomographic set, we have performed simulated experiments with sets having an increasing number of equidistant coherent states, with amplitudes in a given range $\alpha \in [-3,\ 3]$ and spacing $\delta\alpha$. As even a one-dimensional collection of states provides a quorum [40, 41], we concentrated on states with the same phase $\phi = 0$. For each set, the matrix representation of the detector was retrieved solving equation (7), thus building a function $g_k^j(\delta\alpha)$. Since the identity matrix $\mathbb{I}$ is the ideal-case solution of the reconstruction algorithm, we consider the following function of the amplitude spacing $\delta\alpha$

$$\Delta(\delta\alpha) = \mathtt{Tr}\,[\mathbb{I} \cdot g_k^j(\delta\alpha)] \tag{8}$$

as a figure of merit to assess tomographic sets, e.g. to find the minimal $\delta\alpha$ corresponding to a reliable reconstruction. For a perfect reconstruction, the two matrices are both the identity and Δ reduces to the dimension of the matrix $\mathbf{g}$. In the opposite case, more and more elements on the diagonal will be voided, and the trace will decrease. In figure 4 we show the results: a steep transition, corresponding to a deterioration of the reconstruction, appears for $\delta\alpha \simeq 0.7$.

A similar conclusion may be obtained theoretically upon considering the overlap of two Gaussian distributions $p_\sigma(x,\ x_0)$ with the same standard deviation σ and different mean values, i.e.

$$f(y) = \sqrt{\pi} \int_{-\infty}^{+\infty} \mathrm{d}x\ p_\sigma(x,\ x_0)\ p_\sigma(x,\ x_0 + y). \tag{9}$$

In particular, the function $y \cdot f(y)$ may be used to assess the tomographic set of coherent states, as it captures, roughly speaking, the trade-off between an increasing spacing and a decreasing overlap. Upon substituting $\sigma^2 = \frac{1}{4}$, as it is for coherent states, we have that $y \cdot f(y)$ has a maximum at $y_{\max} = 2^{-\frac{1}{2}} \simeq 0.707$, in good agreement with the value obtained by simulated experiments via equation (8). The reliability of this estimation has been then confirmed experimentally (see below).

A similar study was carried out to study the effect of bin size δx in the discretisation of equation (5). As it was found that the change in bin size only affects the resolution of the reconstruction, we selected a value of $\delta x = 0.1$, the standard of our setup for state reconstruction.

4.2. Properties of the tomographic set: robustness

By considering the full tomographic set of coherent states, we then investigated the role of phase noise on our reconstructing algorithm. It is necessary to separate the effect of rescaling, due to the coefficients γ_s, from the quadrature response of the detector, represented by the matrix $\mathbf{g}$. To this aim, the full set of amplitudes $\{\alpha_s\}$ was taken not from the calibrated value, but directly as the mean value of the probability distributions measured with

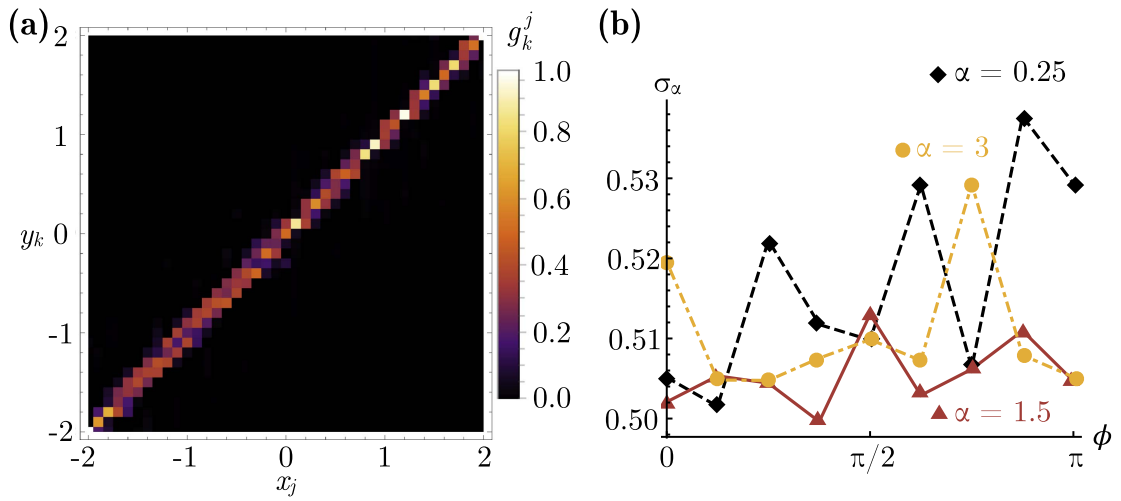

Figure 5. Analysis of the effect of noise in the homodyne detection. Panel (a) presents the reconstructed matrix **g** obtained from the full tomographic set by imposing $|\alpha_s| = |\tilde{\alpha}_s|$. A minimum deviation from the expected diagonal shape is visible. The standard deviations σ_α of the coherent states of the set are reported in panel (b) as a function of phase ϕ, for three of twelve sets of amplitudes: $\alpha = 0.25$ (dashed), $\alpha = 1.5$ (solid), $\alpha = 3.0$ (dotted–dashed).

the homodyne detector, and the coefficient matrix **g** was retrieved imposing $|\tilde{\alpha}_s| = |\alpha_s|$. Every coefficient γ_s is then effectively set to 1, and every uncertainty due to the rescaling is excluded from the detector tomography.

The result of the reconstruction, reported in figure 5(a), show the expected diagonal shape. The standard deviations of the homodyne distributions are reported in figure 5(b). We see some fluctuations, consistent with the expected value of the variance. The locking system of the homodyne detection could introduce an uncertainty in the selected phase ϕ of the quadrature. However, no correlation with the phase of the coherent states may be observed, thus suggesting that phase noise play a minor, if any, role. In order to verify this statement in a quantitative way, and recalling the model presented in equation (3), we described a possible phase noise in the measurement scheme by writing the homodyne distribution of a coherent state $p_\alpha(x)$ as the following convolution

$$p_\alpha^{\sigma_f}(x) = \frac{1}{\pi\sigma_f}\int_{-\infty}^{+\infty} \mathrm{d}\phi\; \mathrm{e}^{-2(x-|\alpha|\cos\phi)^2}\,\mathrm{e}^{-\frac{(\phi-\phi_0)^2}{2\sigma_f^2}}, \tag{10}$$

where σ_f is the standard deviation of the alleged phase noise, and ϕ_0 is the phase of the measured quadrature. Upon applying the reconstruction algorithm of equation (7) to a set of simulated data from equation (10) (with amplitudes and phases equal to the experimental set) we were able to assess the effect of phase noise. The reconstructed matrices **g** are reported in figure 6(a), for increasing values of σ_f. As it is apparent from the plot, already for $\sigma_f = 0.1$, the reconstruction is strongly affected. By comparing these results with figure 5(a), it is possible to exclude any phase noise above $\sigma_f = 0.1$ (i.e. any noise variance above $\sigma_f^2 = 10^{-2}$).

The possible effects of amplitude noise have been analysed in an analogue way, by describing the noise by means of Gaussian convolution with standard deviation σ_a, leading to

$$p_\alpha^{\sigma_a}(x) = \sqrt{\frac{2}{\pi(4\sigma_a^2+1)}}\exp^{-\frac{2(x-\alpha\cos\phi)^2}{4\sigma_a^2+1}}. \tag{11}$$

This is just a new Gaussian with increased total standard deviation given by $\sqrt{\sigma_a^2 + 1/4}$. A new set of coherent states was generated from equation (11), with phases and amplitudes taken from the experimental tomographic set. Three matrices **g** were calculated, for increasing values of σ_a. The results are reported in figure 6(b). As it is apparent from the plot the 'width' of the diagonal increases with the added noise, but the matrices retain their shape, in contrast with the results of figure 6(a).

Upon comparing these results with figure 5(a), and considering the measured standard deviation for the coherent states of figure 5(b), we may bound the amplitude noise at $\sigma_a < 0.1$.

In order to further analyse the possible effects of noise, we noticed that the amplitude convolution of equation (11) maintains the Gaussianity of the coherent state. Moreover, the limit that we have imposed is sufficiently low that we can discard this source of noise in the detector tomography. On the other hand, the convolution of equation (10) distorts the probability distribution $p_{\alpha_s}(x)$, especially for phases around $\pi/2$ and

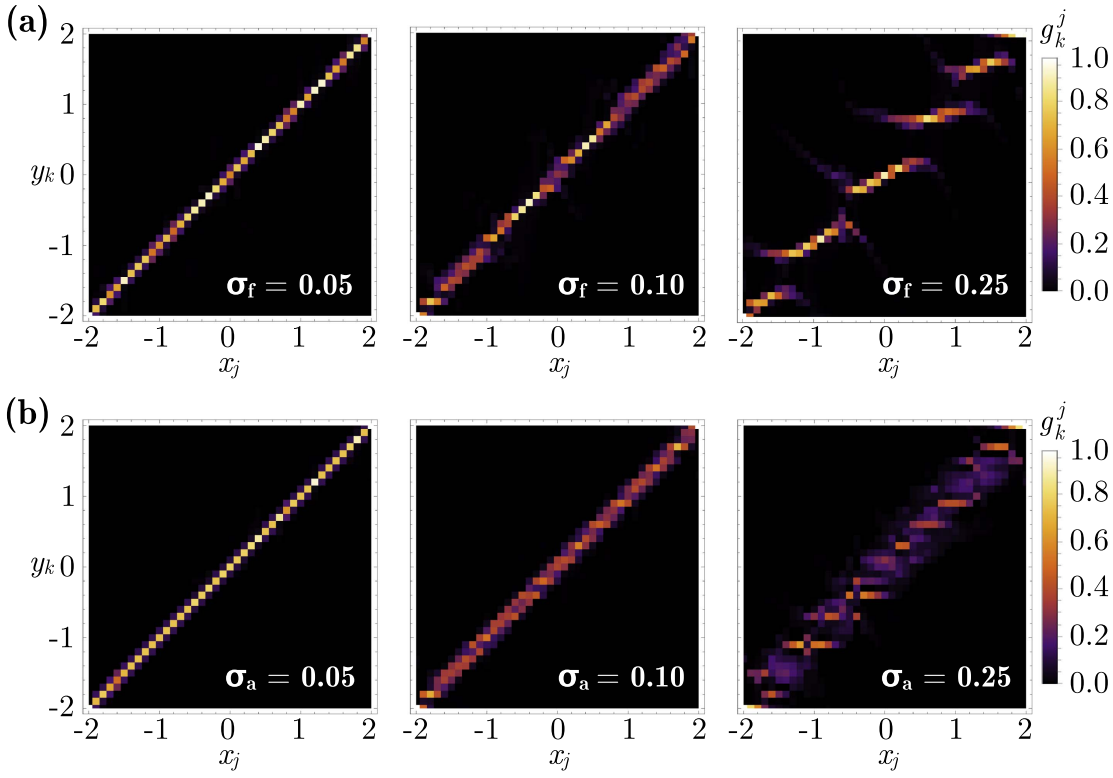

Figure 6. Simulated detector tomographies, assessing the role of phase and amplitude noise on the detector tomography. Panel (a) reports matrices **g** obtained from coherent states with added phase noise, with $\sigma_f = 0.05,\ 0.1,\ 0.25$. Panel (b) reports matrices obtained with coherent states with added amplitude noise, with $\sigma_a = 0.05,\ 0.1,\ 0.25$. In both cases we imposed $|\alpha_s| = |\tilde{\alpha}_s|$.

high amplitudes $|\alpha_s|$. We can then lower the limit on σ_f by looking at the individual probability distributions $p_{\alpha_s}(x)$ of the coherent states. In fact, due to the convolution of equation (10), the distribution of quadrature values is not Gaussian anymore, and this effect can be quantified. We have therefore employed another least-squares algorithm to find the residuals χ^2 for every $p_{\alpha_s}(x)$ with respect to a Gaussian of equal centre α_s and variance $1/4$, the expected result for our choice of normalisation of coherent states. We have then calculated χ^2 for the set of simulated $p_{\alpha_s}^{\sigma_f}(x)$, and compared the two results for increasing values of σ_f. As it is clear from figure 7(a), the residuals show a radically different behaviour for the experimental and for the simulated states. As for the case of figure 5(a), for the experimental data there is no correlation with the phase of the measured quadrature. From the maximum values of χ^2 of the two panels of figure 7(a) we were able to exclude any phase noise above $\sigma_f = 0.075$.

The results reported in figure 7(a) provided a quantitative analysis of the effect of phase noise. As a qualitative comparison comparison, we implemented equation (10). After the LO was locked to the required phase, during the measurement process the actual locking signal was substituted with a Gaussian distribution. The variance was calibrated by measuring the voltage required for a 2π phase change. We set the standard deviation of the added phase noise to 0.25, and we then acquired 12 coherent states, with amplitudes $\alpha_s \in [0,\ 3]$ and equal phase $\phi = 0$. The reconstructed matrix is reported in figure 7(b) and shows a similar behaviour to our simulations of figure 6(a). This result was obtained with a heavy modification of the locking procedure in the homodyne detection, again showing the high sensitivity of the system to phase noise.

At this point, we may avoid any further inquiries on the role of phase noise in the detector tomography, as we found it to be too small to be detected in the experimentally sampled distributions and, more importantly, to affect the tomographic results. As both plots of figure 5(b) and top panel of figure 7(a) shows no correlation with ϕ, in striking contrast with the bottom panel of figure 7(a), no extra dependency on phase was assessed. As a consequence, we can assume that the coefficients γ_s are real numbers and that they are constant for all the quadratures x_ϕ.

4.3. Properties of the tomographic set: optimally reduced set

We have now confirmed the effectiveness of our method and the reliability of our set. Looking back at section 4.1, we selected another one-dimensional collection of coherent state, with the minimum spacing. From the full set of coherent states we picked those with a null or π phase difference between the signal and the LO.

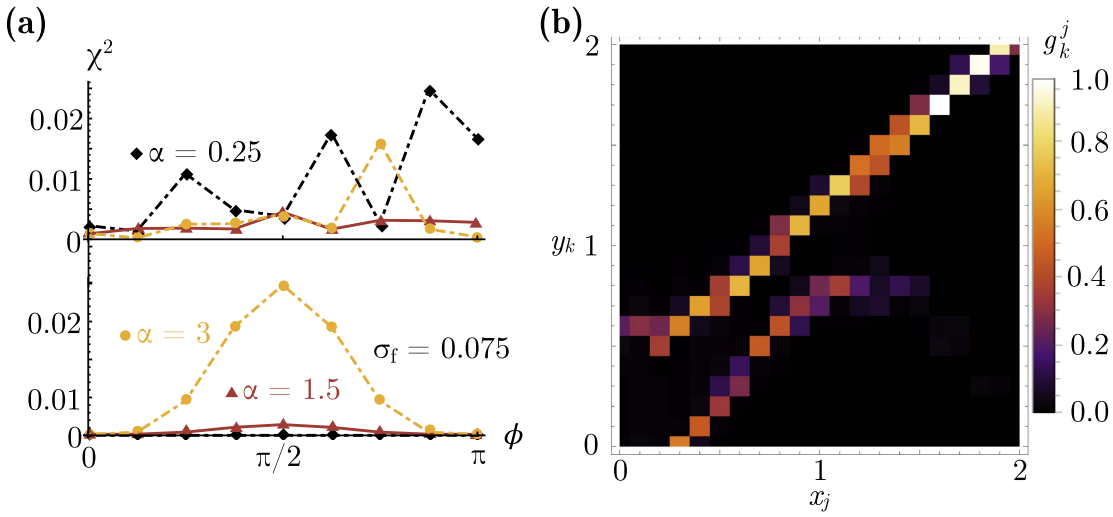

Figure 7. Panel (a) shows the residuals obtained from fitting the experimental set $p_{\alpha_s}(x)$ (top) and a simulated set $p^{\sigma_f}_{\alpha_s}(x)$ (bottom) to Gaussian distributions. Three of the twelve amplitude sets are reported: $\alpha = 0.25$ (dashed), $\alpha = 1.5$ (solid), $\alpha = 3.0$ (dotted–dashed). A new maximum of $\sigma = 0.075$ for Gaussian phase noise can be set. Panel (b) shows the matrix $\mathbf{g}$ obtained with a set of coherent states with an experimentally added phase-noise of $\sigma = 0.25$. The results are in good agreement with figure 6(a).

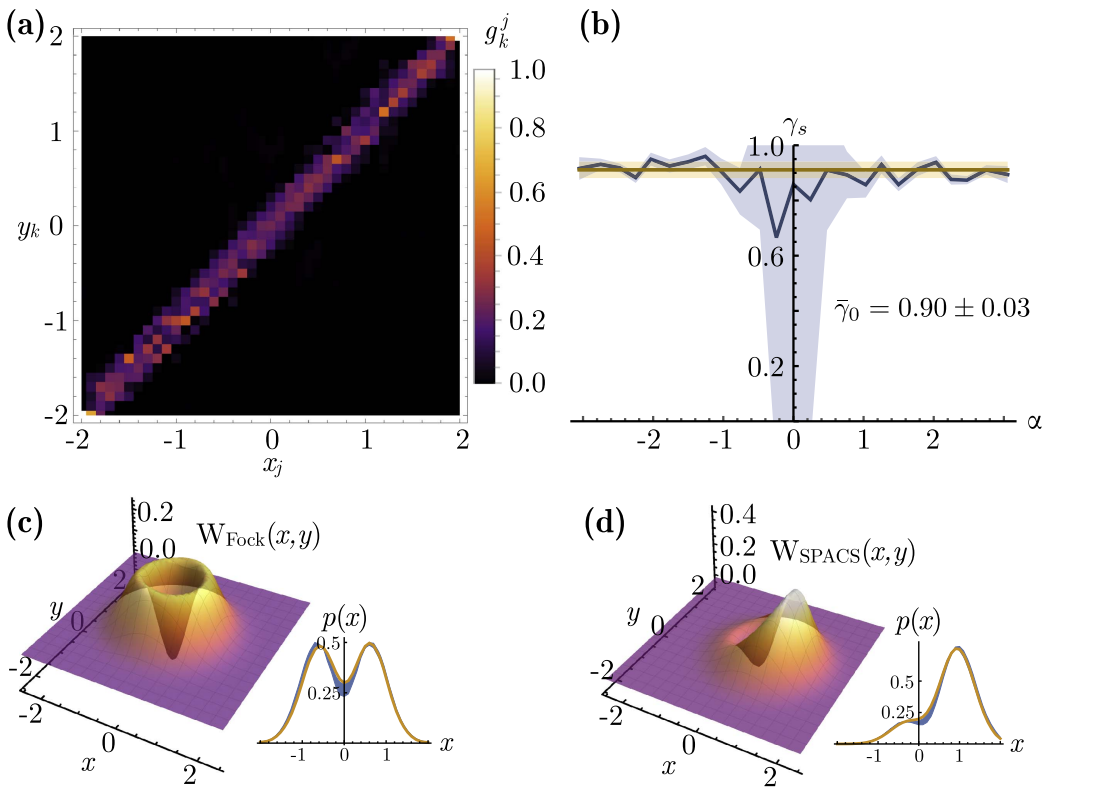

Figure 8. Quantum tomography of a homodyne detector. Panel (a) shows the matrix g_k^j obtained with a reduced set. The array of coefficients γ_s is reported in blue in figure 8(b), with the uncertainty represented by the shaded blue area. In a similar fashion, the mean value $\bar{\gamma}_0$ and its uncertainty are indicated in solid and shaded yellow. In panels (c) and (d) we report the experimentally reconstructed Wigner functions for the Fock state $|1\rangle$ and for a single photon-added coherent state. The side plots in both panels show the Wigner marginal distributions $p(x)$ (yellow), which are both very close to their representations in the detector description $\mathcal{P}(x)$ (the uncertainty due to the spread of $\bar{\gamma}_0$ is given by the blue-shadowed areas).

This set of 25 coherent states was then inserted into the algorithm of equation (7) together with the set of calibrated amplitudes $\{\alpha_s\}$, and the results are shown in figure 8(a). By comparing this matrix with that of figure 5(a) one notices the spread of the coefficients around the diagonal, due to the additional parameters γ_s.

These are reported in blue in the plot of figure 8(b). The uncertainty on the $\{\gamma_s\}$ was obtained by considering the behaviour of equation (7) as a function of γ. The second-order derivative of equation (7) was calculated for every γ_s, and its inverse used as the error, that is represented by the blue-shaded area in figure 8(b). The error on γ_s is increasing for decreasing values of α, since for the limiting case of $\alpha = 0$ our model is not defined. A final value of $\bar{\gamma}_0 = 0.90(3)$ could be obtained with a weighted average.

4.4. POVM validation

The aim of QDT is to fully characterise a given detector by retrieving the set of operators that completely describes its measurement process. In order to validate our technique for QDT, we have employed the reconstructed POVM to reproduce measurements performed on known states. With the apparatus of figure 2 we have generated and characterised by standard quantum homodyne tomography a single-photon Fock state and a SPACS with amplitude 0.5. For both states we have acquired about 10^6 quadrature data for 10 phase values in the interval $[0, \pi]$. An iterative maximum likelihood reconstruction procedure [56–58] is used to retrieve the density matrixes, and the corresponding Wigner functions are shown in figures 8(c) and (d). These experimental Wigner functions are then compared to those obtained for the same states using the reconstructed detector POVM. The photon addition scheme of our setup, fundamental for the generation of these two states, had been previously characterised [46, 59], and the operator $a^\dagger$ had been found to apply to a given input state with preparation efficiency $\zeta \approx 0.91$. The measured quadrature distributions for the Fock state and the SPACS, reported in figures 8(c) and (d), are in excellent agreement with the expected Q-function representation $\mathcal{P}(x)$ based on the tomography of our homodyne detector. For both the Fock state and the SPACS we have recovered the marginal distributions $p(x)$ from the Wigner functions. Considering the fidelity $\mathcal{F}$ defined as $\mathcal{F} = \delta x \sum_j \sqrt{p(x_j)\mathcal{P}(x_j)}$, we found $\mathcal{F} > 0.99$ for both states. The robustness and reliability of our method has thus been confirmed and we have proved that the specific experimental realisation of the detector, which depends on several parameters (like the detector quantum efficiency, the degree of mode matching, the alignment, etc), can be efficiently captured by the tomographic procedure. We also proved that the results of subsequent measurements can be effectively reproduced.

The reduced, one-dimensional tomographic set of coherent states that we have used so far has proved to be a good test for our detectors. In order to improve the accuracy of the reconstruction we may extend the set to cover a bigger portion of phase space, while to minimise the experimental effort we may want to reduce the number of states in the set. Proceeding as above, and following our predictions from equation (8), we found that a minimal set of nine coherent states may be selected from the experimental data, all at phase $\phi = 0$. The amplitude spacing is three times larger than in the previous situation, but the reduced set is still able to provide a quorum for the tomography. Results are presented in figures 9(a) and (b). On the other hand, even with the full set of 109 coherent states we have been able to efficiently reconstruct the detector, despite the increased phase space coverage and the increased fluctuations, due to oversampling.

The matrix g_k^j and the coefficients γ_s for this case are shown in figures 9(c) and (d). On the basis of the previous analysis, and considering the large uncertainty on γ_s in the area close to the origin, we have assigned a fixed value $\gamma_s = 1$ to probe states with amplitudes smaller than 0.5, and we have neglected them in the weighted average. We found that the values of $\bar{\gamma}$ for the smallest and the largest tomographic set are given by $\bar{\gamma}_1 = 0.91(3)$ and $\bar{\gamma}_2 = 0.84(9)$ respectively. In fact, all the values of $\bar{\gamma}_0$, $\bar{\gamma}_1$ and $\bar{\gamma}_2$ are comparable within the uncertainty. On the other hand, they convey different information regarding the detector. The matrices reported in figures 8(a) and 9(a) present an additional spread of the coefficients around the diagonal. This can be considered as an additional rescaling parameter, modelling the experimental fluctuations, that is therefore directly included in the tomography. Values for $\bar{\gamma}$ are then larger, with reduced uncertainty. The matrix of figure 9(c) has instead a smaller spread, and therefore the extra rescaling is conveyed in $\bar{\gamma}_2$, lowering its value and making it more accurate, even though less precise. In this case, $\bar{\gamma}_2$ is better suited to be compared to the value of the detection quantum efficiency η that can be obtained by classical calibration. The overall detection efficiency of our apparatus is $\eta = \eta_d\, \eta_n\, \eta_o\, \eta_m = 0.69(4)$ where the quantum efficiency of the photodiodes is directly measured to be $\eta_d = 0.980(5)$ and the electronic signal to noise ratio ($S = 10.5$ dB) corresponds to an efficiency of $\eta_n = S - 1/S = 0.91(1)$ [60]. The optical losses are $\eta_o = 0.95(1)$, and the non-perfect mode matching between LO and the heralded SPDC signal mode corresponds to $\eta_m = 0.82(1)$ which it is obtained following [52]. Indeed, we find that $\bar{\gamma}_2 \approx \sqrt{\eta}$, despite the fact that our model does not involve any prior knowledge of the detector structure or implementation, i.e. our scheme may be employed for absolute calibration of the detector. Overall, we see that different sets may be exploited to highlight specific properties of the detector, adding value to our technique.

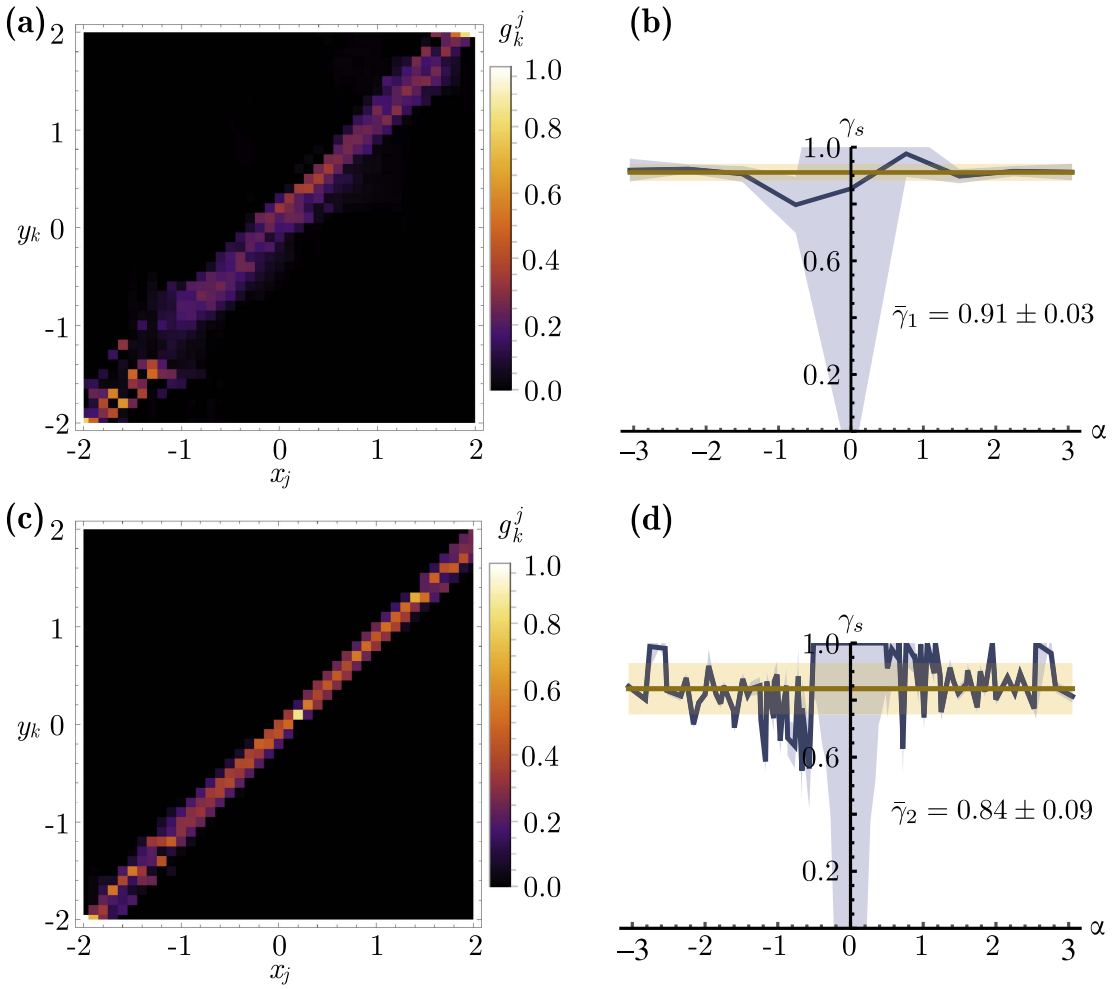

Figure 9. Changing the number of coherent states in the tomographic set. Panels (a) and (b) show results of the tomography for the limiting case of an amplitude spacing of 0.7, as predicted by the theoretical modelling. The limiting case of oversampling was also tested, yielding another positive result. Results of QDT using the full tomographic set of 109 states are reported in panels (c) and (d).

5. Conclusions

We have suggested and demonstrated a QDT technique for a homodyne detector. In ideal conditions each detector operator is associated to a single quadrature projector: our technique suitably describes how experimental noise and specific physical realisations of the detector affect this description and allows us to quantify experimentally the spreading of the detector operators onto adjacent quadrature states. The model is general enough to describe currently used homodyne setups, and it has proven capable of effectively describing the detector response to different tomographic sets. The reconstructed POVM have been then validated on different nonclassical states, thus confirming the robustness and the reliability of the method.

Our results provide a general method to estimate the overall detection efficiency in this class of detectors and may represent a valuable resource to optimise homodyne detection in different situations. Our model may be generalised to specifically treat single parameters of homodyne detectors, as mode mismatch, saturation or correlations between amplitude and phase noise. Besides, a better understanding of the fundamental functioning of this detector paves the way to an evolution of the same, as well as a broader and more precise use in quantum optics and quantum technology with continuous variables.

Acknowledgments

This work has been supported by UniMI through the *H2020 Transition Grant* 15-6-3008000-625 and by MIUR under the initiative *Progetto Premiale: Oltre i limiti classici di misura*. SG acknowledge support by the EU under the ITN *Frontiers in Quantum Technology* (GA 317232). MB and AZ acknowledge the support of Ente Cassa di Risparmio di Firenze.

References

[1] Lvovsky A I and Raymer M G 2009 *Rev. Mod. Phys.* **81** 299–332
[2] D'Ariano G M, Paris M G A and Sacchi M F 2003 *Quantum Tomography (Advances in Imaging and Electron Physics* vol 128*)* ed P W Hawkes (Amsterdam: Elsevier) pp 205–308
[3] Welsch D G, Vogel W and Opatrný T 1999 *Prog. Opt.* **39** 63–211
[4] Vogel K and Risken H 1989 *Phys. Rev.* A **40** 2847–9
[5] Smithey D T, Beck M, Raymer M G and Faridani A 1993 *Phys. Rev. Lett.* **70** 1244–7
[6] D'Ariano G M, Macchiavello C and Paris M G A 1994 *Phys. Rev.* A **50** 4298–302
[7] Armen M A, Au J K, Stockton J K, Doherty A C and Mabuchi H 2002 *Phys. Rev. Lett.* **89** 133602
[8] D'Auria V, Fornaro S, Porzio A, Solimeno S, Olivares S and Paris M G A 2009 *Phys. Rev. Lett.* **102** 020502
[9] Řeháček J, Olivares S, Mogilevtsev D, Hradil Z, Paris M G A, Fornaro S, D'Auria V, Porzio A and Solimeno S 2009 *Phys. Rev.* A **79** 032111
[10] Wittmann C, Andersen U L, Takeoka M, Sych D and Leuchs G 2010 *Phys. Rev.* A **81** 062338
[11] Chi Y M, Qi B, Zhu W, Qian L, Lo H K, Youn S H, Lvovsky A I and Tian L 2011 *New J. Phys.* **13** 013003
[12] Blandino R, Genoni M G, Etesse J, Barbieri M, Paris M G A, Grangier P and Tualle-Brouri R 2012 *Phys. Rev. Lett.* **109** 180402
[13] Kumar R, Barrios E, MacRae A, Cairns E, Huntington E and Lvovsky A I 2012 *Opt. Commun.* **285** 5259–67
[14] Olivares S, Cialdi S, Castelli F and Paris M G A 2013 *Phys. Rev.* A **87** 050303
[15] Jeong H, Zavatta A, Kang M, Lee S W, Costanzo L S, Grandi S, Ralph T C and Bellini M 2014 *Nat. Photon.* **8** 564–9
[16] Berni A A, Gehring T, Nielsen B M, Händchen V, Paris M G A and Andersen U L 2015 *Nat. Photon.* **9** 577–81
[17] Cialdi S, Porto C, Cipriani D, Olivares S and Paris M G A 2016 *Phys. Rev.* A **93** 043805
[18] Mandarino A, Bina M, Porto C, Cialdi S, Olivares S and Paris M G A 2016 *Phys. Rev.* A **93** 062118
[19] Gunawardena M and Elliott D S 2007 *Phys. Rev. Lett.* **98** 043001
[20] Gross C, Strobel H, Nicklas E, Zibold T, Bar-Gill N, Kurizki G and Oberthaler M K 2011 *Nature* **480** 219–23
[21] Verhagen E, Deléglise S, Weis S, Schliesser A and Kippenberg T J 2012 *Nature* **482** 63–7
[22] Cooper M, Karpiński M and Smith B J 2014 *Nat. Commun.* **5** 4332
[23] Řeháček J, Mogilevtsev D and Hradil Z 2010 *Phys. Rev. Lett.* **105** 010402
[24] Fiurášek J 2002 *Phys. Rev.* A **66** 012304
[25] Babichev S A, Brezger B and Lvovsky A I 2004 *Phys. Rev. Lett.* **92** 047903
[26] Kurucz Z, Adam P, Kis Z and Janszky J 2005 *Phys. Rev.* A **72** 052315
[27] Jeong H, Lance A M, Grosse N B, Symul T, Lam P K and Ralph T C 2006 *Phys. Rev.* A **74** 033813
[28] Laghaout A, Neergaard-Nielsen J S, Rigas I, Kragh C, Tipsmark A and Andersen U L 2013 *Phys. Rev.* A **87** 043826
[29] Luis A and Sánchez-Soto L L 1999 *Phys. Rev. Lett.* **18** 3573–6
[30] Fiurášek J 2001 *Phys. Rev.* A **64** 024102
[31] D'Ariano G M, Maccone L and Lo Presti P 2004 *Phys. Rev. Lett.* **93** 250407
[32] D'Ariano G M and Perinotti P 2007 *Phys. Rev. Lett.* **98** 020403
[33] Lundeen J S, Feito A, Coldenstrodt-Ronge H B, Pregnell K L, Silberhorn C, Ralph T C, Eisert J, Plenio M B and Walmsley I A 2009 *Nat. Phys.* **5** 27–30
[34] D'Auria V, Lee N, Amri T, Fabre C and Laurat J 2011 *Phys. Rev. Lett.* **107** 050504
[35] Akhlaghi M K, Majedi A H and Lundeen J S 2011 *Opt. Express* **19** 784–6
[36] Brida G, Ciavarella L, Degiovanni I P, Genovese M, Migdall A, Mingolla M G, Paris M G A, Piacentini F and Polyakov S V 2012 *Phys. Rev. Lett.* **108** 253601
[37] Brida G, Ciavarella L, Degiovanni I P, Genovese M, Lolli L, Mingolla M G, Piacentini F, Rajteri M, Taralli E and Paris M G A 2012 *New J. Phys.* **14** 085001
[38] Zhang L, Coldenstrodt-Ronge H B, Datta A, Puentes G, Lundeen J S, Jin X M, Smith B J, Plenio M B and Walmsley I A 2012 *Nat. Photon.* **6** 364–8
[39] D'Ariano G M, Maccone L and Paris M G A 2001 *J. Phys. A: Math. Theor.* **34** 93–103
[40] Janszky J and Vinogradov A V 1990 *Phys. Rev. Lett.* **64** 2771–4
[41] Janszky J, Domokos P, Szabo S and Adam P 1995 *Phys. Rev.* A **51** 4191–3
[42] Lobino M, Korystov D, Kupchak C, Figueroa E, Sanders B C and Lvovsky A I 2008 *Science* **322** 563–6
[43] Kiesel T, Vogel M W, Parigi V, Zavatta A and Bellini M 2008 *Phys. Rev.* A **78** 021804
[44] Kiesel T and Vogel M W 2010 *Phys. Rev.* A **82** 032107
[45] Kiesel T, Vogel M W, Hage B and Schnabel R 2011 *Phys. Rev. Lett.* **107** 113604
[46] Rahimi-Keshari S, Kiesel T, Vogel W, Grandi S, Zavatta A and Bellini M 2013 *Phys. Rev. Lett.* **110** 160401
[47] Leonhardt U 1997 *Measuring the Quantum State of Light* (Cambridge: Cambridge University Press)
[48] D'Ariano G M, Paris M G A and Sacchi M F 2004 Quantum tomographic methods *Quantum State Estimation* ed M G A Paris and J Řeháček (Berlin: Springer) pp 7–58
[49] Zavatta A, Bellini M, Ramazza P L, Marin F and Arecchi F T 2002 *J. Opt. Soc. Am.* B **19** 1189
[50] Zavatta A, Viciani S and Bellini M 2006 *Laser Phys. Lett.* **3** 3–16
[51] Zavatta A, Viciani S and Bellini M 2004 *Science* **306** 660
[52] Aichele T, Lvovsky A I and Schiller S 2002 *Eur. Phys. J.* D **18** 237–45
[53] Migdall A 1999 *Phys. Today* **52** 41–6
[54] Leonhardt U and Munroe M 1996 *Phys. Rev.* A **54** 3682–4
[55] Sych D, Řeháček J, Hradil Z, Leuchs G and Sánchez-Soto L L 2012 *Phys. Rev.* A **86** 052123
[56] Hradil Z, Řeháček J, Fiurášek J and Ježek M 2004 Maximum-likelihood methods in quantum mechanics *Quantum State Estimation* ed M G A Paris and J Řeháček (Berlin: Springer) pp 59–112
[57] Lvovsky A I 2004 *J. Opt. B: Quantum Semiclass. Opt.* **6** S556–9
[58] Řeháček J, Hradil Z, Knill E and Lvovsky A I 2007 *Phys. Rev.* A **75** 042108
[59] Zavatta A, Viciani S and Bellini M 2004 *Phys. Rev.* A **70** 053821
[60] Appel J, Hoffman D, Figueroa E and Lvovsky A I 2007 *Phys. Rev.* A **75** 035802